

Graphene field-effect transistors as room-temperature terahertz detectors

L. Vicarelli¹, M. S. Vitiello^{1*}, D. Coquillat², A. Lombardo³, A. C. Ferrari³, W. Knap², M. Polini¹, V. Pellegrini¹ and A. Tredicucci¹

The unique optoelectronic properties of graphene make it an ideal platform for a variety of photonic applications¹, including fast photodetectors², transparent electrodes in displays and photovoltaic modules^{1,3}, optical modulators⁴, plasmonic devices⁵, microcavities⁶, and ultra-fast lasers⁷. Owing to its high carrier mobility, gapless spectrum and frequency-independent absorption, graphene is a very promising material for the development of detectors and modulators operating in the terahertz region of the electromagnetic spectrum (wavelengths in the hundreds of micrometres), still severely lacking in terms of solid-state devices. Here we demonstrate terahertz detectors based on antenna-coupled graphene field-effect transistors. These exploit the nonlinear response to the oscillating radiation field at the gate electrode, with contributions of thermoelectric and photoconductive origin. We demonstrate room temperature operation at 0.3 THz, showing that our devices can already be used in realistic settings, enabling large-area, fast imaging of macroscopic samples.

Photodetection of far-infrared radiation (from hundreds of gigahertz to a few terahertz) is important for a variety of potential applications, ranging from medical diagnostics to process control, and homeland security⁸. Terahertz radiation penetrates numerous commonly used dielectric materials, otherwise opaque for visible and mid-infrared light. At the same time, it allows spectroscopic identification of hazardous substances and compounds, through their characteristic molecular fingerprints⁸. Commercially available terahertz detectors are based on thermal sensing elements that are either very slow (10–400 Hz modulation frequency for Golay cells or pyroelectric elements, however capable of reaching noise equivalent powers (NEP) in the 10^{-10} W Hz^{-1/2} range) or require cryogenic cooling (for example 4 K for superconducting hot-electron bolometers)⁹, while those exploiting fast nonlinear electronics (Schottky diodes) are mostly limited to a range below 1 THz (ref. 9).

A more recent approach exploits field-effect transistors (FETs; ref. 10), either as III–V high-electron-mobility transistors or Si-based complementary metal oxide semiconductor (MOS) transistors. These provide excellent sensitivities (NEP in the 10^{-10} – 10^{-11} W Hz^{-1/2} range, depending on temperature and operation frequency), with the intrinsic possibility of high-speed response (in principle just limited by the read-out electronics impedance). This approach was also recently extended to InAs nanowires (NWs) operating at room temperature¹¹ (RT).

Terahertz detection in FETs is mediated by the excitation of plasma waves in the transistor channel¹². On one hand, a strong resonant photoresponse is predicted in materials having plasma damping rates lower than both the frequency, ω , of the incoming

radiation, and the inverse of the electron transit time in the channel. This requires mobilities of at least several thousand cm² (V⁻¹ s⁻¹) at frequencies above 1 THz. Under these conditions, stationary states arising from the quantization of plasma waves over the gate width are excited whenever the gate voltage, V_G , is such that $n\pi s/(2L_G) = \omega$, n being an odd integer, s the plasma-wave velocity, and L_G the gate width. On the other hand, when plasma oscillations are overdamped, a broadband terahertz detection is observed¹⁰. In this case, the oscillating electric field of the incoming radiation applied between source and gate electrodes produces a modulation of both charge density and carrier drift velocity¹². Carriers travelling towards the drain generate a continuous source–drain voltage, Δu , controlled by the carrier density in the channel (see Methods). This can then be maximized by varying V_G close to the peak transconductance point. Resonant photodetection is still to be fully demonstrated at RT, although some evidence was reported for GaAs high-electron-mobility transistors¹³, while large responsivity enhancements with respect to the non-resonant case are still to be achieved.

High mobility at RT is crucial to take full advantage of resonant detection, and to make FET detectors equally performant above 1 THz (refs 14,15). The naturally occurring two-dimensional electron gas in a doped graphene sheet has a very high mobility even at RT (ref. 16). Furthermore, it supports plasma waves¹⁷ that are weakly damped in high-quality samples^{18,19}. Thus, graphene FET (GFET) plasma-based photodetectors could outperform other terahertz detection technologies^{20,21}.

Thus far, the development of graphene-based photodetectors has been limited to the visible to near-infrared range, exploiting the creation of electron–hole pairs following light absorption^{2,5,22–24}. In the terahertz range, however, the photon energy is just a few meV, and light absorption is prevented by Pauli blocking, owing to the unavoidable doping of as-produced graphene samples²⁵, and charge inhomogeneities²⁶. Cryogenic graphene bolometric detectors have also been recently developed, and their operation demonstrated in the mid-infrared²⁷.

Here we demonstrate efficient terahertz detectors working at RT, by combining top-gated GFETs with terahertz receivers designed to achieve the desired sensitivity. When a terahertz oscillating electric field is fed between the gate and the channel of a FET device, the incoming wave is rectified by the nonlinearity of the transfer characteristic. A d.c. signal between source and drain, proportional to the received optical power, is then induced, provided an asymmetry exists between source and drain in the coupling with the radiation²⁸. This can best be achieved by using a low shunt capacitance antenna, with arms connected to gate and source electrodes. Antenna coupling ensures selective responsivity to both the spatial mode and polarization of the incoming radiation. As

¹NEST, Istituto Nanoscienze-CNR and Scuola Normale Superiore, I-56127 Pisa, Italy, ²Laboratoire Charles Coulomb UMR 5221, Université Montpellier 2 and CNRS, F-34095, Montpellier, France, ³Department of Engineering, Cambridge University, Cambridge CB3 0FA, UK. *e-mail: miriam.vitiello@sns.it.

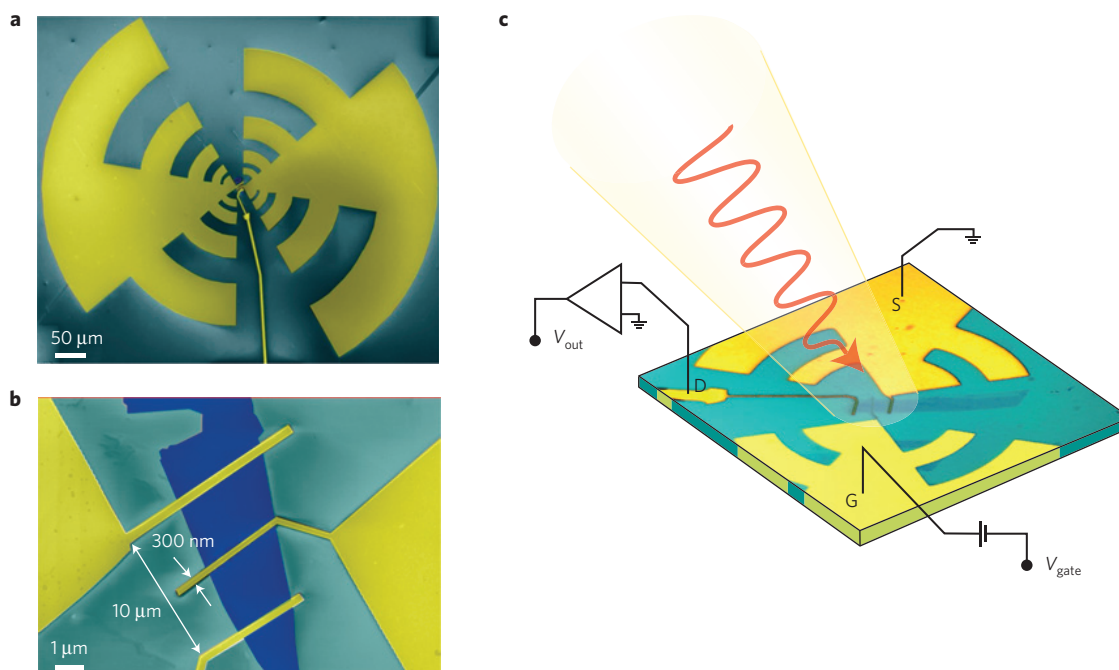


Figure 1 | Antenna-coupled GFET-terahertz detector. **a, b**, False-colour SEM micrographs. The detector consists of a log-periodic circular-toothed antenna patterned between the source and gate of a GFET. The drain is a metal line running to the bonding pad. The channel length is $\sim 10 \mu\text{m}$, with a gate width $L_G \sim 300 \text{ nm}$. A Cr/Au top-gate is patterned in the middle of the graphene channel after atomic-layer deposition of a 35 nm HfO_2 insulating layer. An electromagnetic simulation using finite-elements (Ansoft HFSS) shows that the antenna has resonant frequencies $\sim 0.4, 0.7, 1, 1.4 \text{ THz}$. **c**, The terahertz radiation is focused by off-axis parabolic mirrors.

well as their technological relevance, our GFET-based terahertz detectors have the potential for investigations of fundamental physics. For example, in the weakly-damped limit they may allow one to probe the hydrodynamic behaviour of ‘chiral’ electron plasmas and their nonlinear instabilities^{12,29}. Moreover, bilayer GFETs with narrow top gates are particularly suited to unravel the interplay between photo-excited plasma-wave transport and intriguing effects such as chirality-assisted electronic cloaking³⁰ and Zener-tunnelling-induced negative differential conductivity³¹.

The devices are built as follows. We use graphene exfoliated on Si/SiO₂ (see Methods) and lithographically define a single lobe of a log-periodic circular-toothed antenna¹¹ as source contact, with an outer radius of 322 μm , while the drain is a metal line running to the bonding pad. An identical antenna lobe, acting as top-gate, is then defined by e-beam lithography, after atomic layer deposition of a $\sim 35 \text{ nm}$ thick HfO_2 insulating layer. The channel length is between 7 and 10 μm , while the gate width is $L_G = 200$ or 300 nm, depending on the device. Figure 1 shows scanning electron microscope (SEM) images and a schematic of the antenna-coupled GFET-terahertz detector.

Figure 2a,c plots the conductivity, σ , extracted from the source–drain current (I_{SD}) measured at RT in single- (SLG) and bi-layer (BLG) graphene devices, while sweeping V_G from -1 to $+3.5 \text{ V}$ and keeping the source–drain voltage at $V_{\text{SD}} = 0.1 \text{ mV}$. In both cases, as expected¹⁶, the conductivity as a function of V_G goes through a minimum when the chemical potential below the gate crosses the charge neutrality point (CNP). In both samples, the CNP is located at positive V_G , underlying the p-doping of our samples, consistent with the doping level estimated by Raman measurements³². Note that in our GFETs the gate electrode width is much smaller than the source–drain distance. This implies that, in general, one cannot simply assume the measured resistance to be fully dominated by that of the gated region.

A diffusive model of transport (see Methods) predicts a second-order nonlinear response when an oscillating terahertz

field is applied between gate and source. This implies that the photovoltage Δu is proportional to the derivative of the channel conductivity with respect to V_G :

$$\Delta u \propto \frac{1}{\sigma} \times \frac{d\sigma}{dV_G} \quad (1)$$

Figure 2b,d shows the photovoltage as a function of V_G for the SLG-FET (Fig. 2b) and BLG-FET (Fig. 2d), as inferred from equation (1), using as an input the measured V_G -dependent conductivity: $\sigma = \sigma(V_G)$. In both cases, Δu varies from negative to positive, while crossing the CNP, consistent with the ambipolar nature of transport in graphene¹⁶.

To access the photoresponse, we employ the 0.3 THz radiation generated by an electronic source based on frequency multipliers³³. This is collimated and focused by a set of two $f/1$ off-axis parabolic mirrors. The intensity is mechanically chopped at frequencies between 90 Hz and 1 kHz, and Δu is measured by means of a lock-in amplifier in series with a voltage preamplifier, having an input impedance of 10 M Ω and an amplification factor $G = 1,000$. The vertically polarized incoming radiation impinges on the GFET mounted in a dual-in-line package, with an optical power $P_t = 2.1 \text{ mW}$.

The photoresponse is measured at zero V_{SD} , as a d.c. voltage Δu at the drain, while the source is grounded. The responsivity, R_v , is extracted from the measured Δu as: $R_v = \Delta u S_t / (P_t S_a)$, where S_t is the radiation beam spot area and S_a the active area³³. This definition of R_v assumes that the whole power incident on the antenna is effectively coupled to the GFET. In our case, the relatively high device impedance results in a mismatch with the antenna output ($\sim 100 \Omega$ or lower). It is thus likely that a considerable fraction of the radiation field is not funnelled into the GFET. Thus, our R_v should be considered as lower limits. Given our beam diameter $d = 4 \text{ mm}$, $S_t = \pi d^2 / 4 = 12.6 \times 10^{-6} \text{ m}^2$. As the total area of our device, including antenna and contact pads, is smaller than the

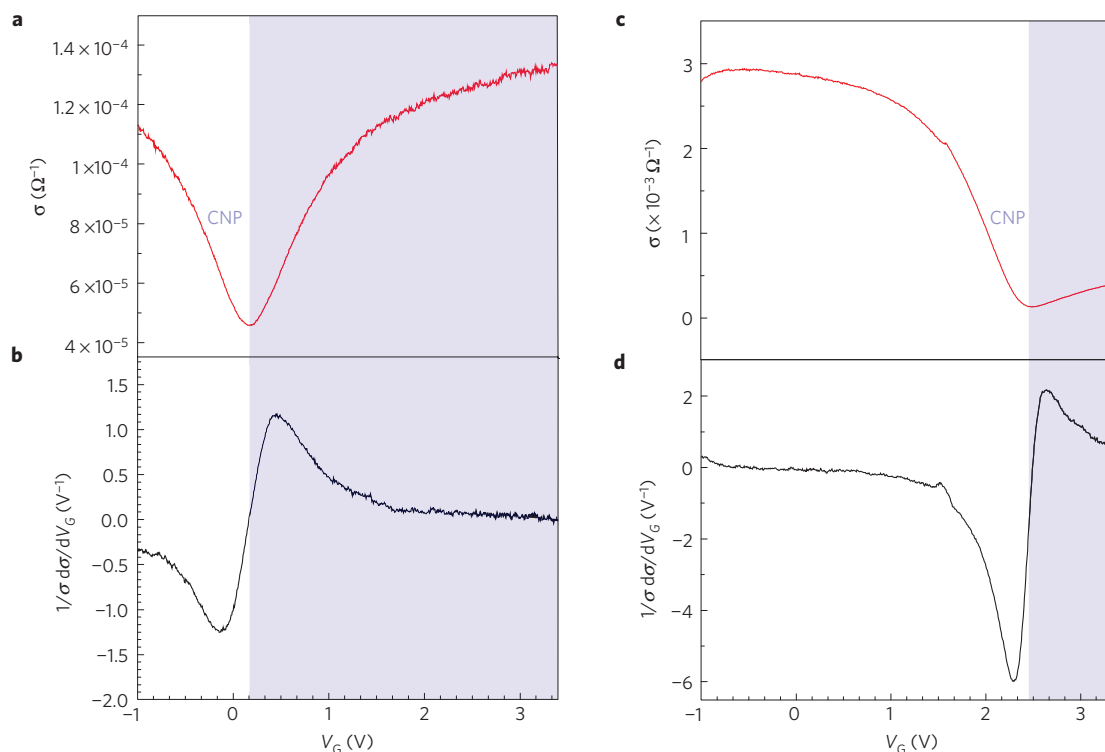


Figure 2 | Device characteristics. **a,c**, RT conductivity as a function of V_G in SLG (**a**) and BLG (**c**) FETs, while keeping $V_{SD} = 0.1\text{mV}$. The drain contact is connected to a current amplifier, to convert the current into a voltage signal with an amplification factor 10^4 V A^{-1} . **b,d**, Derivative of conductivity multiplied by the resistance, as a function of V_G , in SLG (**b**) and BLG (**d**) FETs. This is the expected responsivity following a diffusive model of transport (see Methods). A sign change occurs as V_G crosses the charge neutrality point. The background colour of **a-d** is switched from white to blue at the CNP.

diffraction-limited area $S_\lambda = \lambda^2/4$, we take the active area to be S_λ . The induced Δu is then extracted from the lock-in signal, \mathcal{L} , without correction from the amplifier input load³³:

$$\Delta u = \frac{2\pi\sqrt{2}}{4G}\mathcal{L} \quad (2)$$

where the factor 2 is due to the peak-to-peak magnitude, the factor $\sqrt{2}$ originates from the lock-in amplifier rms amplitude, and $\pi/4$ is the fundamental sine wave Fourier component of the square wave produced by the chopper.

Figure 3a plots the SLG-FET R_v as a function of V_G , while modulating the terahertz source at 500 Hz. Each curve corresponds to a different relative orientation between the source electric-field polarization and the antenna axis. The photoresponse drops rapidly with angle until it becomes almost zero when the incoming polarization is orthogonal to the antenna axis, confirming the efficacy of our dipole antenna. The dependence of Δu on V_G is in qualitative agreement with the trend in Fig. 2b, thereby proving that our detectors operate in the broadband overdamped regime. Note that the sign of the photovoltage changes abruptly in the vicinity of the CNP, following the switch of sign of the derivative $d\sigma/dV_G$.

We also note a further sign switch around $V_G = 0$ in all curves. This suggests a contribution to the photoresponse of thermoelectric origin^{23,24}, arising from the presence of the ungated p-doped graphene regions, and subsequent formation of p–p–p or p–n–p junctions, depending on V_G . It is likely that, owing to the presence of the antenna, the electronic distribution near the junction between gate and source is more effectively ‘heated’ by the incoming radiation, either through free-carrier (Drude-like) absorption, or indirectly from the lattice. The resulting thermoelectric voltage should have the same functional dependence as in equation (1), but with opposite sign, plus a roughly gate-independent value,

determined by the thermoelectric Seebeck coefficient of the ungated graphene region^{23,24}. It should thus change sign near $V_G = 0$, where the carrier density in the gated and ungated regions becomes exactly the same, as the sign of the difference between the thermoelectric coefficients across the junction switches, as discussed in ref. 24. The gate-independent term also gives rise to rigid offsets between measurements, where the temperature difference induced between the junctions is not the same, as may for instance be the case when the antenna orientation is varied.

The precise shape and absolute values of the responsivity curves tend to vary from measurement to measurement and with gate-bias sweep direction, owing to the GFET hysteretic behaviour. Our devices reach $R_v \sim 100\text{ mV W}^{-1}$, with no clear dependence on chopper modulation frequency up to 1 kHz. A quantitative evaluation of the thermoelectric contribution is presently difficult, mainly because it has the same functional dependence on V_G as in equation (1). For plasma waves in the overdamped regime, R_v is determined by the relative change of conductivity with V_G . However, to extract the absolute R_v , one should precisely know the antenna coupling efficiency, which is hard to compute with high accuracy. For a qualitative estimate, we can use the numbers fit to the responsivity of other FET detectors with similar antenna designs measured in the same experimental set-up³⁴. These give coupling efficiencies $\sim 0.05\text{--}0.1\text{ V}^2\text{ W}^{-1}$, which, multiplied by the maximum values of $\sigma^{-1} \times d\sigma/dV_G$ from Fig. 2b, give peak $R_v \sim 0.07\text{--}0.15\text{ V W}^{-1}$, in good agreement with the measured R_v .

Figure 3b plots R_v as a function of V_G in a BLG-FET, while modulating the terahertz source at 500 Hz. The measured shape of the R_v curve is in excellent agreement with that predicted by the diffusive plasma-wave detection model (see Fig. 2d), up to the CNP (at $\sim 2.5\text{ V}$). However, no change of sign is seen at the CNP, and a response strongly enhanced with respect to that predicted by equation (1) appears for V_G larger than the CNP, when the device

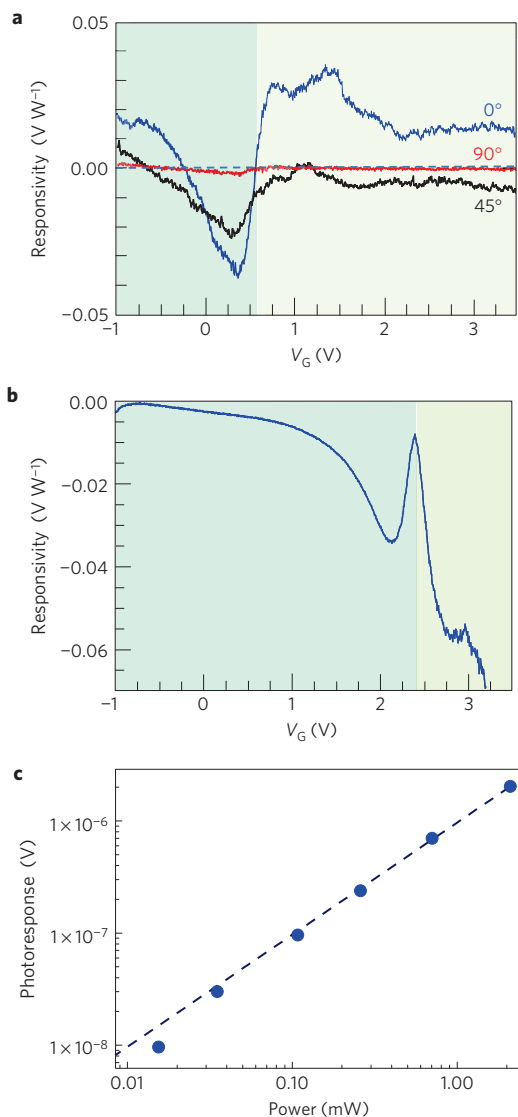


Figure 3 | Responsivity. **a,b**, RT responsivity as a function of V_G for detectors based on SLG-FET (with data for different angles between the beam polarization axis and the antenna axis) (**a**) and BLG-FET (**b**). A dashed line marks the zero value of output voltage. Different background colours identify regions below and above the CNP. **c**, Photoresponse signal of the BLG-FET at $V_G = 0.2$ V as a function of incident terahertz power. Dots are the experimental data; the dashed line is a fit to the data.

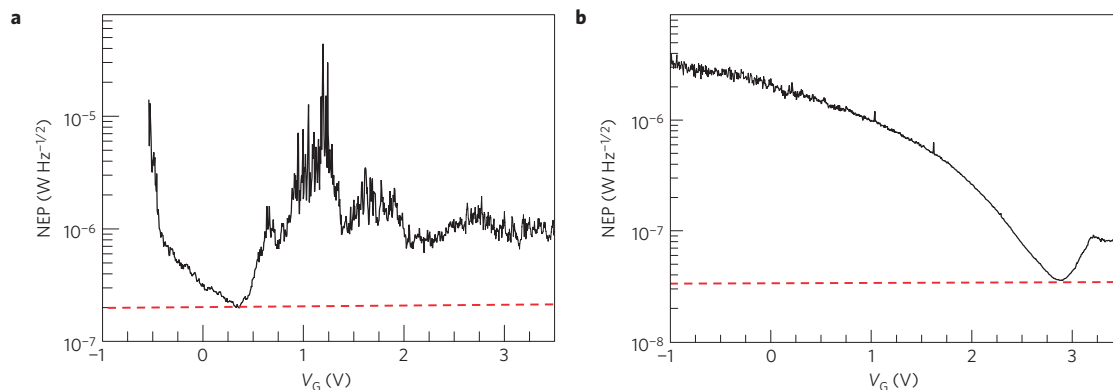


Figure 4 | NEP. NEP as a function of V_G for detectors based on SLG-FET (**a**) and BLG-FET (**b**), assuming a noise level dominated by the thermal Johnson–Nyquist contribution $N = \sqrt{4k_B T/\sigma}$. A red horizontal line is drawn at the value of minimum NEP.

is in the p–n–p configuration. This suggests an additional contribution to the photovoltage, this time of constant sign. Its magnitude grows rapidly with V_G , eventually dominating in the regime in which a p–n–p junction is present. The photovoltage is noisier above the CNP, implying an additional intrinsic noise mechanism. We assign this to interband transitions driven by the terahertz field at the p–n junction, with the resulting generation–recombination noise. This contribution, only seen in BLG, may be related to the higher density of states near the Dirac point, or a bandgap opening due to the electric field, with the terahertz field possibly adding a gap modulation. Whatever the precise origin, this leads to a maximum $R_p \sim 150$ mV W⁻¹, significantly higher than R_v due to the broadband plasma response. We also note that, as expected, the detectors response at any given V_G is linear with the incident terahertz power, as exemplified in Fig. 3c for the BLG device.

From the application perspective, the relevant figure of merit to characterize a photodetector is the NEP, which corresponds to the lowest detectable power in a 1 Hz output bandwidth (or equivalently a 0.5 s integration time): the lower the NEP, the better the detector. The noise level of FET detectors is dominated by the thermal Johnson–Nyquist contribution¹⁰ $N = \sqrt{4k_B T/\sigma}$, which can be directly extracted from the measured conductivity. The NEP is then obtained dividing this value by R_v . Figure 4a,b plots our measured NEPs as functions of V_G . The minimum RT NEP is ~ 200 nW Hz^{-1/2} for SLG and almost one order of magnitude lower (~ 30 nW Hz^{-1/2}) for BLG. This difference is expected in view of the higher responsivity of the latter, combined with its higher conductivity (translating into lower noise). We note that such numbers are in fact upper limits, as they refer to the signal power incident on the device as a whole (optical NEP), that is, they are not corrected for the coupling efficiency of the radiation into the nano-sized transistor element, which is probably very low in our present configuration. Such corrections would then give much smaller NEPs. Thus, care must be taken when comparing optical NEP values with those derived from the signal power actually absorbed in the detector (electrical NEP), used for example to describe the mid-infrared cryogenic bolometers of ref. 27. Previous RT FET detectors based on InAs NWs achieved optical NEPs $\sim 10^{-9}$ W Hz^{-1/2} (ref. 11), while Si n-MOSs reached $\sim 10^{-11}$ W Hz^{-1/2} (ref. 10). The reason why our devices have higher NEPs stems from the higher R_v enabled by the current on-off ratio of the highly mature Si complementary metal oxide semiconductors technology, exceeding 10^5 . Thus, a possible path to improve performance is to enhance the GFET peak transconductance. This should be feasible, as higher mobilities could be achieved by perfecting the fabrication approach, for example by placing graphene on BN substrates³⁵. Moreover, the decrease of channel resistance will reduce noise and improve

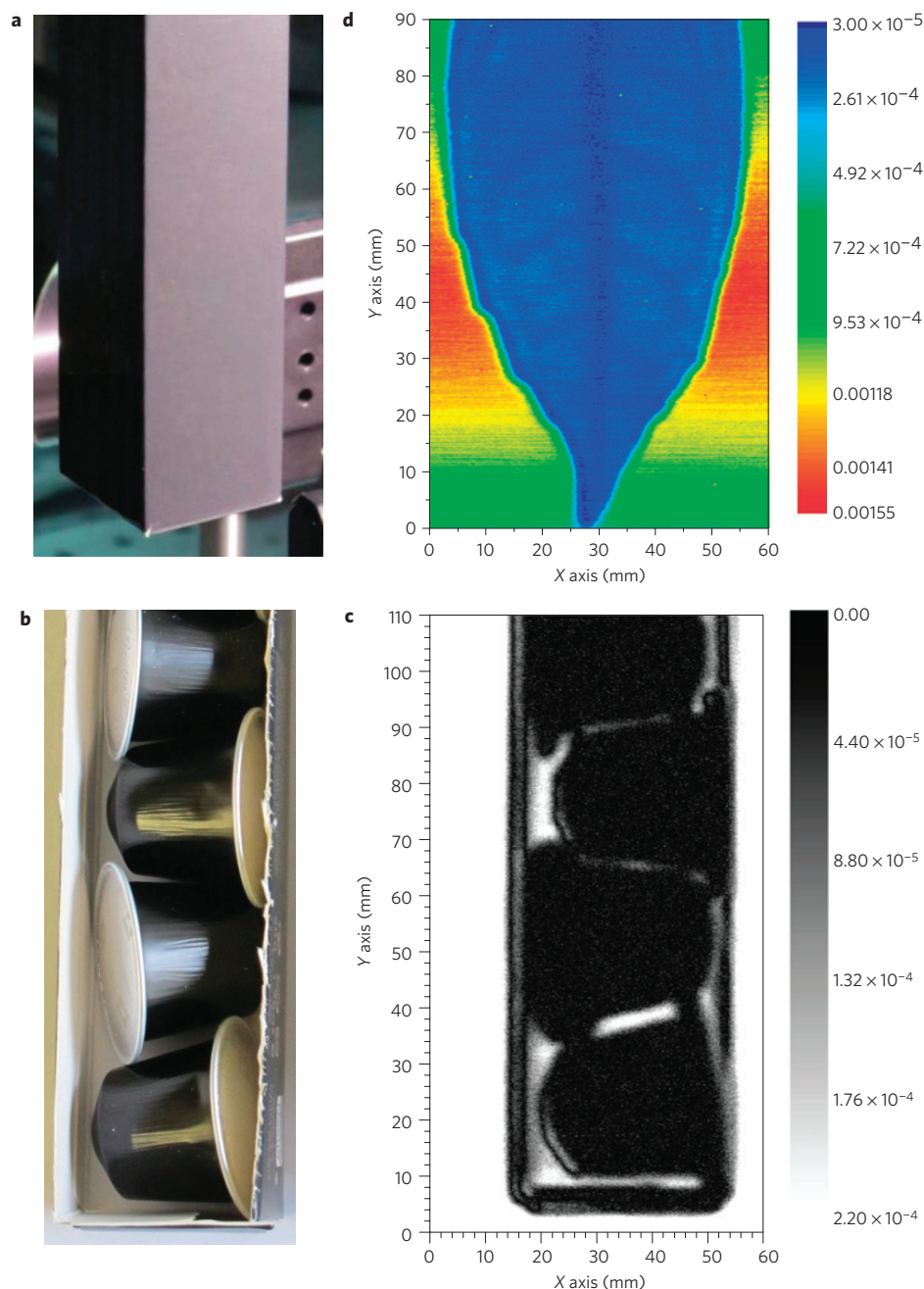


Figure 5 | Fast, large-area, RT, terahertz imaging. **a**, Photograph of a closed coffee-capsule box. For visible light illumination the contents cannot be seen, either by naked eye or by the CCD camera used to take the picture. **b**, same box as in **a**, but with one side removed. This allows the inside of the box to be seen, but requires the destruction of the packaging. **c**, 0.3 THz transmission image of the sealed, intact box shown in **a**, measured at RT with a GFET mounted on a XY stage, with spatial resolution $\sim 0.5 \mu\text{m}$. Comparing **c** with **b**, it is clear that our graphene-based terahertz detector allows one to monitor the contents of the closed package. **d**, 0.3 THz image of a leaf. Our detector not only images the sample, but also reveals the leaf veins.

matching with the antenna. The design of the antenna could also be improved, including coupling optics and optimization of the substrate thickness. Further advances are expected by achieving the resonant detection regime, and also by understanding and exploiting the new physics emerging in BLG samples, which may lead to even better device concepts.

In any case, our devices are already exploitable, for example for large-area fast imaging. As test object we used coffee capsules (aluminium foil) inside a cardboard box. Figure 5 shows the terahertz image, consisting of 200×550 scanned points, collected by raster-scanning the object in the beam focus, with an integration time of 20 ms per point. The coffee capsules, as well as the air gaps

between them, show clearly in the terahertz image, with a reasonably good spatial resolution. A transmission image of a fresh leaf is also reported in Fig. 5d, allowing us to detect the leaf veins. This shows that our devices are beyond proof-of-concept and can already be used in a realistic setting, enabling large-area, fast imaging of macroscopic samples.

Methods

Device fabrication and characterization. SLG and BLG flakes are produced by mechanical exfoliation of Kish graphite on a highly intrinsic ($\rho = 10 \text{ k}\Omega \text{ cm}$) Si substrate with 300 nm SiO_2 (ref. 36). The number of layers is identified by a combination of optical microscopy³⁷ and Raman spectroscopy³⁸. The latter is also used to

monitor the sample quality by measuring the D to G intensity ratio³⁹ and the doping level³². The selected SLG or BLG flakes are then spin-coated with e-beam sensitive resist. Contact patterns are exposed by e-beam lithography, to make the drain and source contacts. Cr(5 nm)/Au(80 nm) Ohmic contacts are then evaporated onto the samples, followed by lift-off in heated acetone. This results in contact resistivities $\sim 10^{-5} \Omega \text{ cm}^2$. Successive fabrication steps define the top gates, after atomic layer deposition (ALD) of a 35 nm HfO_2 dielectric gate. Owing to the hydrophobic nature of graphene, a functionalization layer needs to be placed before ALD can start. A metallic Cr/Au top-gate is then patterned in the middle of the channel. We extract a top-gate capacitance per unit area $\sim 300\text{--}500 \text{ nF cm}^2$, assuming a dielectric constant $\kappa = 13\text{--}19 \text{ nF cm}^{-2}$ for amorphous HfO_2 . Raman spectra measured before and after HfO_2 deposition show no significant D peaks, indicating no significant degradation of the graphene properties^{38,39}. The electrical characterization is performed by connecting the drain contact to a current amplifier and converting the current into a voltage signal with an amplification factor of 10^4 V A^{-1} .

Diffusive transport model. When the frequency of the impinging radiation ω is such that $\omega\tau_{ee} \ll 1$, with $1/\tau_{ee}$ the electron–electron scattering rate, the electron gas in the channel follows the laws of hydrodynamics^{12,29}. Electrons undergo many collisions with each other during one period of oscillation of the external field, thus establishing a local thermodynamic equilibrium. The timescale associated with electron–electron collisions in graphene is $\sim 1\text{--}10 \text{ fs}$ (ref. 40). In the present experiment $\omega/(2\pi) = 0.3 \text{ THz}$, meaning that $\omega\tau_{ee} \approx 2 \times 10^{-3}\text{--}2 \times 10^{-2}$. In this regime, electrons move collectively, establishing plasma waves in the channel, which are however strongly damped because $\omega\tau_{tr} \ll 1$. Here τ_{tr} is the transport time, which can be estimated from the field-effect mobility to be in the tens of fs. In the hydrodynamic regime, the photoresponse can be calculated by using a one-dimensional model based on Ohm's law,

$$j(x, t) = \sigma E(x, t) = -\sigma \frac{\partial V_G(x, t)}{\partial x} \quad (3)$$

in conjunction with the continuity equation:

$$\frac{\partial[-en(x, t)]}{\partial t} + \frac{\partial j(x, t)}{\partial x} = 0 \quad (4)$$

The total carrier density $-en(x, t)$ is modulated by the gate voltage $V_G(x, t)$ according to

$$-en(x, t) = CV_G(x, t) \quad (5)$$

with C the gate-to-channel capacitance per unit area. The d.c. conductivity σ depends on total carrier density and thus on $V_G(x, t)$, by virtue of equation (5).

Substituting equations (3) and (5) in equation (4) we find:

$$C \frac{\partial V_G(x, t)}{\partial t} - \frac{\partial}{\partial x} \left[\sigma \frac{\partial V_G(x, t)}{\partial x} \right] = 0 \quad (6)$$

We now seek solutions of the differential equation (6) of the form³⁴:

$$V_G(x, t) = U_0 + U_1(x, t) + U_2(x) \quad (7)$$

with the following boundary conditions: $U_1(x=0, t) = U_a \cos(\omega t)$, $U_1(x=L_G, t) = 0$, $U_2(x=0) = 0$, and $U_2(x=L_G) = \text{const}$. We solve equation (6) perturbatively, by expanding σ in a power series. Because $\partial V_G(x, t)/\partial x$ starts at order U_1 , we can stop the expansion of σ at first order in U_1 :

$$\sigma = \sigma(U_0) + \left. \frac{d\sigma(V_G)}{dV_G} \right|_{V_G=U_0} U_1(x, t) \quad (8)$$

The equation for $U_1(x, t)$ is then derived by inserting the Ansatz equation (7) in equation (6) and retaining only terms of order U_1 . We find the following diffusion equation:

$$C \frac{\partial U_1(x, t)}{\partial t} - \sigma(U_0) \frac{\partial^2 U_1(x, t)}{\partial x^2} = 0 \quad (9)$$

The solution of this equation with the above boundary conditions is:

$$U_1(x, t) = U_a \exp(-\kappa x) \cos(\omega t - \kappa x) \quad (10)$$

with $\kappa = \omega C / [2\sigma(U_0)] \gg 1/L_G$.

We now need to find the equation for $U_2(x)$ by retaining all second-order terms. This gives:

$$\frac{d}{dx} \left[\sigma(U_0) \frac{dU_2(x)}{dx} + \left. \frac{d\sigma(V_G)}{dV_G} \right|_{V_G=U_0} \left\langle U_1(x, t) \frac{\partial U_1(x, t)}{\partial x} \right\rangle \right] = 0 \quad (11)$$

where $\langle \dots \rangle$ means average over one period $T = 2\pi/\omega$ of the terahertz field. We thus need to compute the following quadrature:

$$\frac{1}{T} \int_0^T dt U_1(x, t) \frac{\partial U_1(x, t)}{\partial x} = -\frac{1}{2} \kappa U_a^2 \exp(-2\kappa x) \quad (12)$$

In summary, we find

$$U_2(x) = \frac{U_a^2}{4} \frac{1}{\sigma(U_0)} \left. \frac{d\sigma(V_G)}{dV_G} \right|_{V_G=U_0} [1 - \exp(-2\kappa x)] \quad (13)$$

Evaluating the previous expression at $x = L_G$ and taking the limit $L_G \gg \kappa^{-1}$ we finally derive the following expression for the source–drain photovoltage:

$$\Delta u = \frac{U_a^2}{4} \frac{1}{\sigma(U_0)} \left. \frac{d\sigma(V_G)}{dV_G} \right|_{V_G=U_0} \quad (14)$$

Received 10 April 2012; accepted 3 August 2012; published online 9 September 2012

References

- Bonaccorso, F. *et al.* Graphene photonics and optoelectronics. *Nature Photon.* **4**, 611–622 (2010).
- Xia, F., Mueller, T., Lin, Y. M., Valdes-Garcia, A. & Avouris, P. Ultrafast graphene photodetector. *Nature Nanotech.* **4**, 839–843 (2009).
- Bae, S. *et al.* Roll-to-roll production of 30-inch graphene films for transparent electrodes. *Nature Nanotech.* **4**, 574–578 (2010).
- Liu, M. *et al.* A graphene-based broadband optical modulator. *Nature* **474**, 64–67 (2011).
- Echtermeyer, T. J. *et al.* Strong plasmonic enhancement of photovoltage in graphene. *Nature Commun.* **2**, 458 (2011).
- Engel, M. *et al.* Light-matter interaction in a microcavity-controlled graphene transistor. *Nature Commun.* **3**, 906 (2012).
- Sun, Z. *et al.* Graphene mode-locked ultrafast laser. *ACS Nano* **4**, 803–810 (2010).
- Mittleman, D. *Sensing with Terahertz Radiation* (Springer, 2003).
- Sizov, F. & Rogalski, A. Thz detectors. *Prog. Quantum Electron.* **34**, 278–347 (2010).
- Knap, W. *et al.* Field effect transistors for terahertz detection: Physics and first imaging applications. *J. Infrared Millim. TeraHz Waves* **30**, 1319–1337 (2009).
- Vitiello, M. S. *et al.* Room-temperature terahertz detectors based on semiconductor nanowire field-effect transistors. *Nano Lett.* **12**, 96–101 (2012).
- Dyakonov, M. & Shur, M. Shallow water analogy for a ballistic field effect transistor: New mechanism of plasma wave generation by dc current. *Phys. Rev. Lett.* **71**, 2465–2468 (1993).
- Teppie, F. *et al.* Room-temperature plasma waves resonant detection of sub-terahertz radiation by nanometer field-effect transistor. *Appl. Phys. Lett.* **87**, 052107 (2005).
- Nadar, S. *et al.* Room temperature imaging at 1.63 and 2.54 THz with field effect transistor detectors. *J. Appl. Phys.* **108**, 054508 (2010).
- Preu, S., Kim, S., Verma, R., Burke, P. G. & Sherwin, M. S. An improved model for non-resonant terahertz detection in field-effect transistors. *J. Appl. Phys.* **111**, 024502 (2012).
- Geim, A. K. & Novoselov, K. S. The rise of graphene. *Nature Mater.* **6**, 183–191 (2007).
- Liu, T., Willis, R. F., Emtsev, K. V. & Seyller, T. Plasmon dispersion and damping in electrically isolated two-dimensional charge sheets. *Phys. Rev. B* **78**, 201403 (2008).
- Bostwick, A. *et al.* Observation of plasmarons in quasi-freestanding doped graphene. *Science* **328**, 999–1002 (2010).
- Yan, J. *et al.* Observation of magnetophonon resonance of Dirac fermions in graphite. *Phys. Rev. Lett.* **105**, 227401 (2010).
- Ryzhii, V. Terahertz plasma waves in gated graphene heterostructures. *Jpn. J. Appl. Phys.* **45**, L923–L925 (2006).
- Rana, F. Graphene terahertz sources and amplifiers. *IEEE Trans. Nanotech.* **7**, 91–99 (2008).
- Lemme, M. C. *et al.* Gate-activated photoresponse in a graphene p–n junction. *Nano Lett.* **11**, 4134–4137 (2011).
- Song, J. C. W., Rudner, M.S., Marcus, C. M. & Levitov, L. S. Hot carrier transport and photocurrent response in graphene. *Nano Lett.* **11**, 4688–4692 (2011).
- Gabor, N. M. *et al.* Hot-carrier-assisted intrinsic photoresponse in graphene. *Science* **334**, 648–652 (2011).
- Casiraghi, C., Pisana, S., Novoselov, K. S., Geim, A. K. & Ferrari, A. C. Raman fingerprint of charged impurities in graphene. *Appl. Phys. Lett.* **91**, 233108 (2007).
- Martin, J. *et al.* Observation of electron hole puddles in graphene using a scanning single-electron transistor. *Nature Phys.* **4**, 144–148 (2008).

27. Yan, J. *et al.* Dual-gated bilayer graphene hot-electron bolometer. *Nature Nanotech.* **7**, 472–478 (2012).
28. Laisauskas, A. *et al.* Rational design of high-responsivity detectors of terahertz radiation based on distributed self-mixing in silicon field-effect transistors. *J. Appl. Phys.* **105**, 114511 (2009).
29. Landau, L. D. & Lifshitz, E. M. *Fluid Mechanics* (Pergamon, 1966).
30. Gu, N., Rudner, M. & Levitov, L. Chirality-assisted electronic cloaking of confined states in bilayer graphene. *Phys. Rev. Lett.* **107**, 156603 (2011).
31. Nandkishore, R. & Levitov, L. Common-path interference and oscillatory Zener tunneling in bilayer graphene p–n junctions. *Proc. Natl Acad. Sci. USA* **108**, 14021–14025 (2011).
32. Das, A. *et al.* Monitoring dopants by Raman scattering in an electrochemically top-gated graphene transistor. *Nature Nanotech.* **3**, 210–215 (2008).
33. Tauk, R. *et al.* Plasma wave detection of terahertz radiation by silicon field effects transistors: Responsivity and noise equivalent power. *Appl. Phys. Lett.* **89**, 253511 (2006).
34. Sakowicz, M. *et al.* Terahertz responsivity of field effect transistors versus their static channel conductivity and loading effects. *J. Appl. Phys.* **110**, 054512 (2011).
35. Dean, C. R. *et al.* Boron nitride substrates for high-quality graphene electronics. *Nature Nanotech.* **5**, 722–726 (2010).
36. Novoselov, K. S. *et al.* Two-dimensional atomic crystals. *Proc. Natl Acad. Sci. USA* **102**, 10451–10453 (2005).
37. Casiraghi, C. *et al.* Rayleigh imaging of graphene and graphene layers. *Nano Lett.* **7**, 2711–2717 (2007).
38. Ferrari, A. C. *et al.* Raman spectrum of graphene and graphene layers. *Phys. Rev. Lett.* **97**, 187401 (2006).
39. Cancado, L. G. *et al.* Quantifying defects in graphene via Raman spectroscopy at different excitation energies. *Nano Lett.* **11**, 3190–3196 (2011).
40. Polini, M. *et al.* Plasmons and the spectral function of graphene. *Phys. Rev. B* **77**, 081411 (2008).

Acknowledgements

We thank A. H. MacDonald, S. Roddaro and V. Piazza for very fruitful discussions. We acknowledge funding from MIUR-FIRB grant no. RBFR10M5BT and grant no. RBFR10LULP, MISE-ICE grant TERAGRAPH, GIS-TERALAB, GDR2987, GDR-I terahertz, the Region Languedoc-Roussillon, the ERC grant NANOPOTS, EU grants RODIN and GENIUS, a Royal Society Wolfson Research Merit Award, EPSRC grants EP/G030480/1 and EP/G042357/1, and the Cambridge Nokia Research Centre.

Author contributions

M.S.V., A.C.F., W.K., V.P. and A.T. devised the experiments. L.V., M.S.V., D.C. and A.L. performed the experiments. M.S.V., D.C., A.C.F., M.P., V.P. and A.T. analysed and modelled the data. M.S.V., A.C.F., M.P., V.P. and A.T. wrote the paper.

Additional information

Reprints and permissions information is available online at www.nature.com/reprints. Correspondence and requests for materials should be addressed to M.S.V.

Competing financial interests

The authors declare no competing financial interests.